



Technical Note

Detection of Surface Rocks and Small Craters in Permanently Shadowed Regions of the Lunar South Pole Based on YOLOv7 and Markov Random Field Algorithms in SAR Images

Tong Xia , Xuancheng Ren, Yuntian Liu, Niutao Liu * , Feng Xu and Ya-Qiu Jin

The Key Laboratory of Information Science of Electromagnetic Waves (MoE), Fudan University, Shanghai 200433, China; yqjin@fudan.edu.cn (Y.-Q.J.)

* Correspondence: ntlou@fudan.edu.cn

Abstract: Excluding rough areas with surface rocks and craters is critical for the safety of landing missions, such as China's Chang'e-7 mission, in the permanently shadowed region (PSR) of the lunar south pole. Binned digital elevation model (DEM) data can describe the undulating surface, but the DEM data can hardly detect surface rocks because of median-averaging. High-resolution images from a synthetic aperture radar (SAR) can be used to map discrete rocks and small craters according to their strong backscattering. This study utilizes the You Only Look Once version 7 (YOLOv7) tool to detect varying-sized craters in SAR images. It also employs the Markov random field (MRF) algorithm to identify surface rocks, which are usually difficult to detect in DEM data. The results are validated by optical images and DEM data in non-PSR. With the assistance of the DEM data, regions with slopes larger than 10° are excluded. YOLOv7 and MRF are applied to detect craters and rocky surfaces and exclude regions with steep slopes in the PSRs of craters Shoemaker, Slater, and Shackleton, respectively. This study proves SAR images are feasible in the selection of landing sites in the PSRs for future missions.

Keywords: crater detection; rocks; lunar south pole; PSR; SAR



Citation: Xia, T.; Ren, X.; Liu, Y.; Liu, N.; Xu, F.; Jin, Y.-Q. Detection of Surface Rocks and Small Craters in Permanently Shadowed Regions of the Lunar South Pole Based on YOLOv7 and Markov Random Field Algorithms in SAR Images. *Remote Sens.* **2024**, *16*, 1834. <https://doi.org/10.3390/rs16111834>

Academic Editor: Roberto Orosei

Received: 10 April 2024

Revised: 13 May 2024

Accepted: 16 May 2024

Published: 21 May 2024



Copyright: © 2024 by the authors. Licensee MDPI, Basel, Switzerland. This article is an open access article distributed under the terms and conditions of the Creative Commons Attribution (CC BY) license (<https://creativecommons.org/licenses/by/4.0/>).

1. Introduction

Exploration of water ice in the permanently shadowed regions (PSRs) of the lunar poles has become one of the main topics in future lunar missions [1–5]. In the Chinese Chang'e 7 mission [6], a mini-flyer is planned to fly into the PSRs for in situ water ice detection. Surface rocks and small craters in the PSRs will endanger the safety of the mini-flyer. Detecting the distribution of rocks and small craters in the PSRs is necessary.

As there is no direct solar illumination, high-resolution optical images of the PSRs are not available. High-resolution digital elevation models (DEMs) acquired by lunar orbit laser altitude (LOLA) onboard the Lunar Reconnaissance Orbital (LRO) [7] are able to describe the lunar topography. The resolution of DEM data can reach 5 m/pixel near the lunar pole. Median-averaging is used to produce the binned DEM data [7]. Thus, some discrete surface rocks and small craters might be averaged out from the data. In contrast, strong scatterings from the surface rocks and crater walls can be identified in high-resolution synthetic aperture radar (SAR) images. Electromagnetic waves are sensitive to undulations caused by rocks on the lunar surface [8–12]. Rocky regions can be identified in SAR images [13]. The miniature radio frequency (Mini-RF) onboard the LRO acquires SAR images of the entire moon, which can be used to detect craters and rocks [14].

Current studies mainly use DEMs to automatically detect craters in the PSRs [15]. In SAR images, it can be observed that the strong scattering that comes from the crater walls facing the radar has incidence, and the scattering becomes much weaker at the walls facing away from the radar [9,10]. Thus, a crater appears as a semi-bright and semi-dark circular shape. Conventional detection algorithms, such as Canny and Hough detection [16],

cannot be directly applied to the recognition of craters and multi-scaled morphology in SAR images.

Recently, convolutional neural networks (CNNs) have been applied to detect objects in SAR images [17]. But the structure of a CNN is simple, which limits its ability to effectively detect multi-sized objects due to overfitting [17]. By optimizing the network structure and introducing multi-scale techniques [18], the detection algorithm You Only Look Once version 7 (YOLOv7) has proven to be an effective tool for detecting objects of various sizes. In this paper, the YOLOv7 is utilized to detect craters of various sizes in SAR images. The results are analyzed in comparison with the DEMs and optical images. Furthermore, using the Markov random field (MRF) algorithm [19,20], the distribution of surface rocks and pixel-sized craters is identified. As a validation, optical images outside of the PSRs are used. The distribution of surface rocks and small-sized craters at the lunar south pole is detected by YOLOv7 and MRF. The slope angle map generated from the DEM data is used to exclude areas with slopes larger than 10° . The detection result of the preferred landing areas of the Chang'e 7 mission, such as the crater Shackleton in Figure 1, is presented as an example [6]. The geometric distortion of the crater Shackleton caused by the topography in SAR images is corrected using DEM data before detection. The distributions of surface rocks, small craters, and areas with steep slopes in the PSRs of craters Shoemaker and Slater in Figure 1 are analyzed as well.

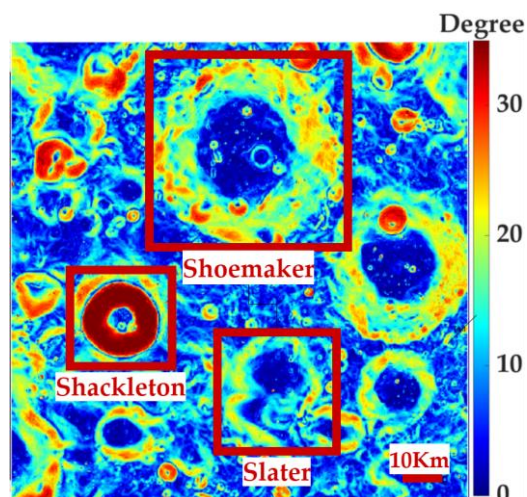


Figure 1. DEM image (118 m/pixel) of the lunar south polar region. Craters Shackleton, Shoemaker, and Slater are included in the red box.

The remaining parts of this paper are organized as follows: Section 2 introduces the YOLOv7 and MRF algorithms for rocky detection. In Section 3, YOLOv7 and MRF are used to detect surface rocks and small craters in the PSRs of the lunar south pole. The detection results of the craters Shackleton, Shoemaker, and Slater are presented. Section 4 gives the conclusions.

2. Methods

2.1. Crater Detection with YOLOv7

2.1.1. YOLOv7 Algorithm

Because of its fast detection speed and high accuracy, YOLOv7 is widely used in target detection [18]. To increase the network's learning capability, YOLOv7 uses the extended efficient layer aggregation network as its backbone computational module [18]. Additionally, it adopts techniques such as expansion, shuffling, and merging bases. YOLOv7 utilizes group convolution to increase the channel number and scale of the computational modules, enabling computational blocks to capture different features. Composite model scaling techniques are incorporated to preserve the model's initial attributes and optimal structure.

Moreover, YOLOv7 adds multiple trainable performance optimization modules to increase training rates while controlling training costs [18,21].

2.1.2. Crater Detection

The YOLOv7 model is used for crater detection. The training and testing datasets consist of SAR images from the Mini-RF, optical images from the Lunar Reconnaissance Orbiter Camera (LROC), and DEM data from LOLA onboard the LRO [7,14,22]. The slope angle map from DEM data is used for the training and testing datasets. The frequency of SAR is 2.38 GHz. The first Stokes parameter, which represents the total backscattering intensity, is used. The incidence angle of the radar is approximately 49° [14]. The experiment is conducted using an NVIDIA GeForce RTX 3090 GPU with 16 GB of memory. The epoch of training is 1000, so the loss function will converge.

The process of dataset production and enhancement is listed as follows:

1. Dataset preparation: The images used as a training set and a testing set were all collected from the lunar pole regions on QuickMap (<https://quickmap.lroc.asu.edu/>).
2. Image cropping: Large SAR images and slope angle maps have a spatial resolution ranging from 60 to 120 m/pixel. These large images were cropped into 500 small images with a size of 600×600 pixels. The initial labeling process involved manual annotation.
3. Dataset division: The 80% labeled images were used as input for model training.
4. YOLO auxiliary marking: Data augmentation techniques were applied to further enhance the train dataset. The trained model was used to label another 25 large SAR images and 25 large slope angle maps automatically. Some manual refinements were made to obtain accurate labels.
5. Image cropping: The labeled large images were subsequently cropped into 1000 small images with a size of 600×600 pixels.
6. Dataset division: Then, both the dataset of 1500 cropped SAR images and 1500 cropped slope angle maps were randomly divided into a training set and a test set in the ratio of 8:2.

In this process, some large craters with diameters greater than 600 pixels in the images could not be completely contained within any of the segmented sub-images. The segmented labels of large craters will be lost.

The detection results of the SAR images outside of the PSRs are compared with optical images and slope angle maps to evaluate the effectiveness of SAR images in detecting craters. In Figure 2a, the spatial resolution of the DEM data is 20 m/pixel. The size of the image is 160×160 pixels. In Figure 2b,c, the spatial resolution of SAR images and optical images is 8 m/pixel with a size of 400×400 pixels. The white arrow in Figure 2b indicates the direction of incidence. The crater walls facing the radar exhibit strong backscattering, while the crater walls facing away from the radar show low backscattering. The YOLOv7 model learns this feature to recognize the shape of the crater. From the slope angle map in Figure 2a, the shape characteristics of the crater can be determined using YOLOv7. The crater walls have steep slopes; the circle-shaped crater can be identified by YOLOv7. Figure 2c shows the optical image for validation.

The large craters within the red circles in Figure 2a are detected in the DEM data by YOLOv7, while some small craters within the blue circles are detected additionally in SAR images with YOLOv7 in Figure 2b. There are pixel-sized craters in box 1 of the SAR image, which cannot be detected by YOLOv7. These craters can be detected by the MRF algorithm in the following content. In Figure 2a, noise or errors are present in box 2 on the slope angle map. In box 2, there are bright spots in Figure 2a, but no undulation was found in the optical image in Figure 2c. The bright spots are likely noise from the DEM data.

To evaluate the accuracy of the YOLOv7 algorithm, the precision and recall of the trained model are analyzed. Precision is the ratio of true positive predictions to the total number of positive predictions made by the model. Recall is the ratio of true positive predictions to the total number of actual positive instances in the dataset [23]. They are standard metrics for

determining detection accuracy [18]. In this experiment, when the intersection over union threshold is 0.44, the highest precision is 91% and the recall is 80% in the test set.

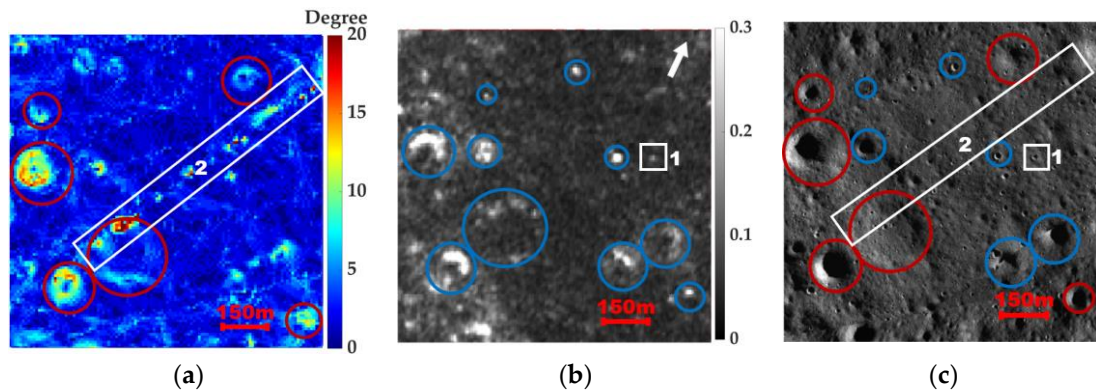


Figure 2. The detection performance of YOLOv7 in DEM data and SAR images: (a) DEM data (20 m/pixel) with detected craters circled in red; (b) SAR image with detected craters circled in blue; The direction of the arrow in the top-right corner indicates the radar illumination direction. (c) optical image used as a validated sample. The central latitude and longitude of the depicted region are 84.73°S and 90.87°E. For verification purposes, these circles are manually labeled on the optical image. Images are from the QuickMap website (<https://quickmap.lroc.asu.edu/>).

2.2. Rocky Area and Pixel-Sized Crater Detection with MRF

2.2.1. MRF Method

MRF can be used for SAR image classification [24]. The classes of pixels in an image are correlated with the adjacent regions. According to the MRF algorithm [25], a pixel belonging to the class ω_k is likely to be surrounded by pixels belonging to the same class [25].

Let the set $C = \{C_\ell, 1 \leq \ell \leq L\}$ represent the possible sets of the class labels in the image, where $C_\ell = \{C_\ell(i, j), 1 \leq i \leq I, 1 \leq j \leq J\}$, $C_\ell(i, j) \in \{\omega_1, \omega_2, \dots, \omega_n\}$, $L = n^I$, n is the number of classes, and I and J are the height and width of the image, respectively. $C_\ell(i, j)$ represents the class label of the pixel (i, j) .

To reduce the error in classification, the posterior conditional probability should be maximized according to the Bayes rule [19].

$$C_o = \arg \max_{C_\ell \in C} \{P(C_\ell | X)\} = \arg \max_{C_\ell \in C} \{P(C_\ell)p(X | C_\ell)\} \quad (1)$$

where C_o represents the set of the class labels in the image when achieving the optimal solution, X represents the whole image, $P(C_\ell)$ is the prior probability for the class labels, and $P(X | C_\ell)$ is the joint probability density function of the pixel values in the image given the set of class labels C_ℓ . The solution to Equation (1) requires the MRF approach to estimate both $P(C_\ell)$ and $P(X | C_\ell)$. Here, MRF-based segmentation models are used to calculate $P(C_\ell)$ and $P(X | C_\ell)$ [20]. The maximum posterior conditional probability $P(C_\ell | X)$ can be obtained by taking the logarithm of Equation (1):

$$C_o = \arg \max_{C_\ell \in C} \{\log(P(C_\ell)) + \log(p(X | C_\ell))\} \quad (2)$$

In this paper, C_ℓ is assumed as the MRF [19,20]. According to the Hammersley–Clifford theorem, MRF can be described by the Gibbs distribution [25]. The probability distribution is approximated based on the number of surrounding labels of each type [20]:

$$P(C_\ell) = \frac{1}{Z} \exp\left(-\frac{E(C_\ell)}{T}\right) \quad (3)$$

where Z is a normalizing constant, and there is

$$Z = \sum_{C_\ell} \exp\left(-\frac{E(C_\ell)}{T}\right) \quad (4)$$

Here, T is set at 1 [20]. $E(C_\ell)$ is the energy function [20]:

$$E(C_\ell) = \frac{\sum_{m=1}^8 v_m(C_\ell(i,j), C_\ell(g,h))}{8} \quad (5)$$

$v_m(C_\ell(i,j), C_\ell(g,h))$ represents whether the class labels belonging to the neighborhood are equal to the class label of pixel (i, j) [19,20], and there is

$$v_m(C_\ell(i,j), C_\ell(g,h)) = \begin{cases} 1, & C_\ell(i,j) = C_\ell(g,h) \\ -1, & C_\ell(i,j) \neq C_\ell(g,h) \end{cases} \quad (6)$$

where $(g, h) \in N(i, j)$. $N(i, j) = \{N_1^{(i,j)}, N_2^{(i,j)}, N_3^{(i,j)}, N_4^{(i,j)}, N_5^{(i,j)}, N_6^{(i,j)}, N_7^{(i,j)}, N_8^{(i,j)}\}$ represents the neighboring pixels of (i, j) .

The pixel values of each class label in the image are assumed to follow a Gaussian distribution [19,20]:

$$p(X | C_\ell) = \frac{1}{\sqrt{2\pi}\sigma_k} \exp\left(-\frac{(x - u_k)^2}{2\sigma_k^2}\right) \quad (7)$$

where $k \in (1, 2 \dots, n)$, k is the label of a certain class, u_k represents the average grayscale value of pixels under a certain class label, and σ_k represents the variance of grayscale value of pixels belonging to class k .

MRF is an unsupervised method. At the first step, each pixel is assigned a random initial value of label. Equations (3) and (7) are used to calculate the prior and likelihood probabilities of a pixel belonging to each class label. Then, these values are substituted into Equation (2) to calculate the posterior probability for each class. The class of a pixel is determined by selecting the class with the highest posterior probability. The steps above are performed iteratively until the result converges. The number of iterations is set to 15, which is sufficient for convergence.

2.2.2. Rock Detection

Rocks on the lunar surface produce strong backscattering in SAR images. The MRF algorithm can be used to detect these rocky areas.

In Figure 3, there is a crater located at 29.733°S, 120.123°E, with a diameter of 1.2 km. The SAR image (14.8 m/pixel) in Figure 3a aligns with the optical image (2 m/pixel) in Figure 3b. The fresh crater and ejecta blanket exhibit strong backscattering in Figure 3a. It can be observed that the ejecta region is bright in optical images with a high solar elevation angle as well. Binary classification is used in MRF. The detection result is shown in Figure 3c.

To validate the classification results of the MRF algorithm, the probability density function (pdf) of the flat regions and rocky regions is presented in Figure 4. The difference between lunar rocky areas and flat regions can be seen in the pdfs in Figure 4. The mean value of the first stokes parameter of the rock areas is 0.54 (−2.68 dB), while the mean value of the flat regions is 0.14 (−8.55 dB). The average backscatter intensity of rocky areas is four times larger than that of flat regions. The overlapping area of the probability distributions for the flat and rock regions in Figure 4 is 3% of the area of either distribution. The overlap between the two pdf curves in Figure 4 is small, which makes it possible to separate them.

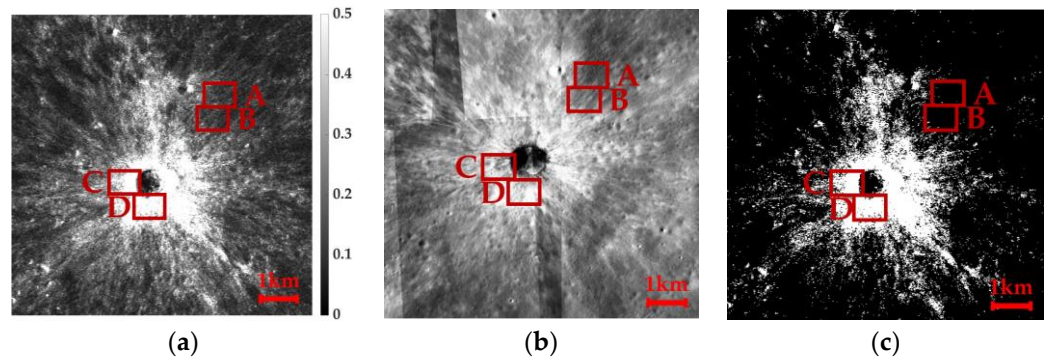


Figure 3. The detection and validation of MRF in SAR images: (a) the SAR image (14.8 m/pixel); (b) a high-resolution optical image (2 m/pixel); (c) the result of detection using the MRF 2 classification algorithm with the SAR image.

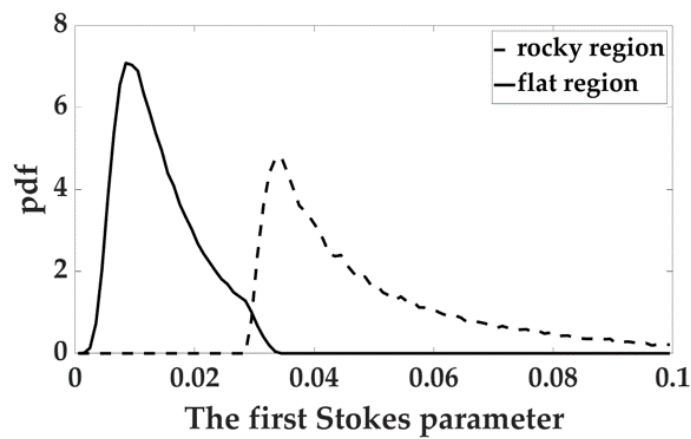


Figure 4. MRF 2 classification pdf of SAR images of a fresh crater.

Figure 5a–d are enlarged images of the red boxes in Figure 3 for further validation. Figure 5a,b show the relatively flat lunar surface. There are almost no large rocks in this area, so the MRF algorithm identifies this area as flat in Figure 3c. Figure 5c,d show large rocks within the ejecta blanket. The bright ejecta blanket is covered by a layer of fresh material, resulting in strong backscattering. The rocks are visible in these images. The area is identified as rough by the MRF algorithm in Figure 3c.

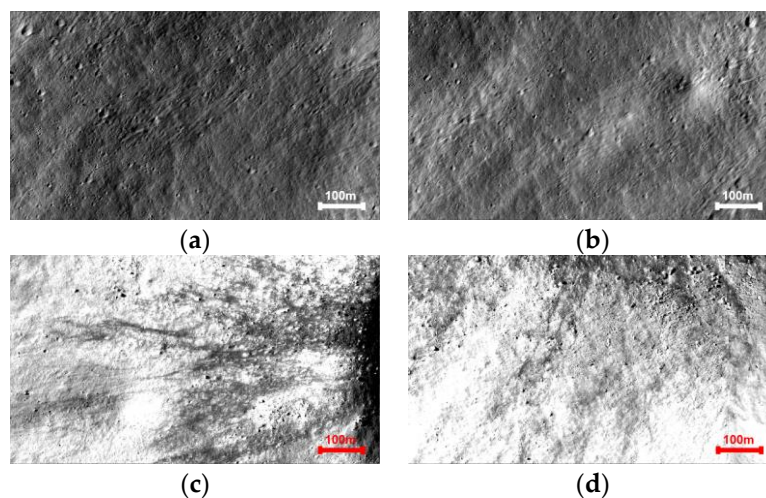


Figure 5. Optical image from the red box in Figure 3b. The resolution is 0.5 m/pixel. Optical images of the flat areas from red boxes A (a) and B (b) in Figure 3. Optical image of the ejecta regions from red boxes C (c) and D (d) in Figure 3.

2.2.3. Pixel-Sized Crater Detection

Figure 6a–d show the aligned slope angle map (14.8 m/pixel), SAR image (14.8 m/pixel), and optical image (2 m/pixel) of a region with small craters at 87.50°S, 110.53°E. Figure 6a shows the original SAR image. The aligned slope angle map from the LOLA DEM of 10 m/pixel is shown in Figure 6b [7]. Small craters with a size of several pixels, which are included in the red and blue circles in the optical images in Figure 6d, are difficult to recognize in the slope angle map in Figure 6b. In the SAR images, small craters have strong backscattering, appearing as bright spots. These bright spots can be extracted by MRF, as shown in Figure 6c. The red masks are the detection results of MRF. The corresponding positions of small craters extracted by MRF in SAR images are manually marked in Figure 6c,d with blue circles. SAR images can identify these small craters that are difficult to recognize in DEM data. There is undulation in box 1 in the optical image in Figure 6d. The undulation can be identified with MRF in box 1 in the SAR image in Figure 6c and cannot be seen in the DEM data in Figure 6b. However, compared with the optical image, there are still some pixel-sized craters, e.g., in box 2, that cannot be detected in the SAR image. In addition, there are some other undulations detected by MRF (red regions) in Figure 6c that are not included in the blue circles for further discussion.

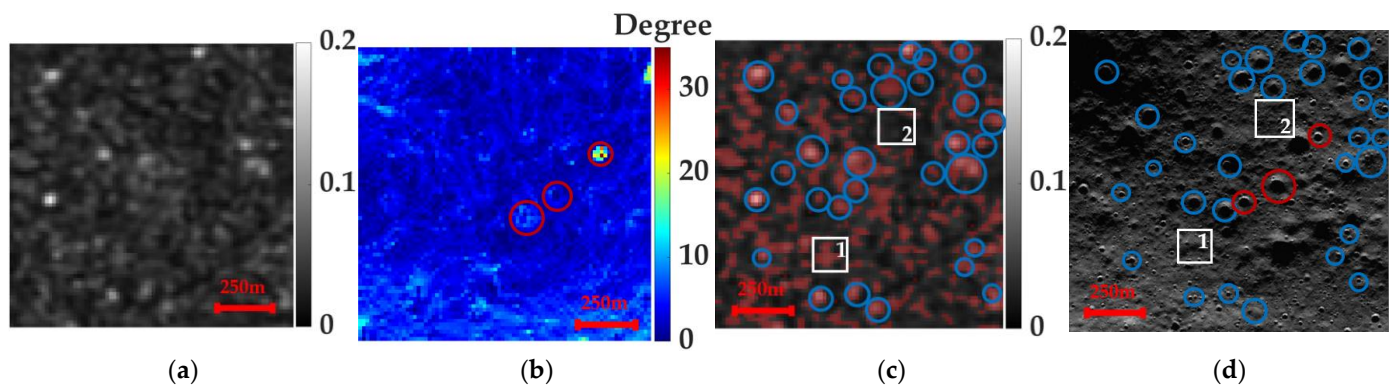


Figure 6. Detection and validation of pixel-sized craters using the MRF algorithm in SAR images: (a) original SAR image (14.8 m/pixel) with a size of 80×80 pixels; (b) DEM data (14.8 m/pixel) with craters manually circled with red; (c) SAR image with a detected result masked by red and manually circled with blue; (d) high-resolution optical image (2 m/pixel) as a validated sample. Blue circles are detected from SAR images and red ones from DEM data.

3. Results

In order to highlight the performance of YOLOv7, a comparative analysis with traditional object detection methods is presented. The average precision (AP) value and the inference speed of the YOLOv7 algorithm are compared with those of Faster-RCNN [26], Cascade-RCNN [27], and YOLOx [28] in Table 1. Those methods are conducted on the platform of MMDetection [29]. The same dataset is used in training and testing. The batch size is 8. AP@.5 presents the precision at different recall levels using a specific intersection over union threshold of 0.5 [23]. The inference speed shows the time cost of each image with a size of 600×600 pixels. As shown in Table 1, the performance of YOLOv7 is better than other methods according to AP@0.5 and inference speed.

Table 1. Comparison with other methods.

Method	AP@.5	Inference Speed (s)
Faster-RCNN	0.650	0.8647
Cascade-RCNN	0.657	0.2853
YOLOx	0.660	0.0731
YOLOv7	0.738	0.0192

The YOLOv7 and MRF are applied to detect the rough rocky regions and craters in SAR images of the lunar south pole in Figure 7a. The incidence angle of the Mini-RF is approximately 49° [14]. Some large crater walls facing away from the radar may exhibit weak backscattering and cannot be detected in SAR images. The aligned DEM data in Figure 7b are used to rule out steep crater walls with slope angles larger than 10° [30,31]. A surface slope of less than 10° is generally considered safe for landing [30]. The detection results for the lunar south pole are shown in Figure 7c. The red masks in Figure 7c are the identified craters, rocks, and areas of large slopes. Figure 7d–f are the enlarged images of crater Idel'son L in box 1 in Figure 7a–c. Figure 7g–i are the enlarged images of the region in box 2 in Figure 7a–c. The rocky regions, craters, and large slope regions are masked by red. The red line in Figure 7d,g represents the boundary between the rocky areas and the flat regions.

Figure 8a shows the craters detected by YOLOv7 with SAR images. Detected craters are included in the red lines. The center and radius of craters can be detected by YOLOv7. Here, 55 craters can be detected by YOLOv7 in the SAR images in Figure 8a. The diameters of the detected craters range from 0.98 to 6.45 km. Moreover, missed craters can be detected by the MRF algorithm with SAR images or by the slope angle maps.

Figure 8b shows the strong backscattering from rocky regions and craters detected by the MRF algorithm with SAR images. The fresh crater with the ejecta blanket in box 1 and the pixel-sized craters or undulations in box 2 cannot be detected in the slope angle map. However, both the ejecta blanket and pixel-sized craters exhibit strong backscattering, which can be extracted by the MRF algorithm in SAR images.

Figure 8c illustrates the regions with slope angles greater than 10° . The backscattering walls of giant craters in box 3 and the slopes in box 4 cannot be identified in the SAR image, but these regions can be extracted from the slope angle map.

In Figure 8, the crater Idel'son cannot be detected by YOLOv7 in Figure 8a, but it can be detected by using MRF and the slope angle map in Figure 8b,c. The craters in box 5 in Figure 8 are difficult to detect with MRF and DEMs. But these craters can be detected by using YOLOv7. The superimposed effect of the three methods is shown in Figure 7c; the red mask indicates the detected rough areas. The areas without the red mask are flat.

In Figure 7g–i, the enlarged data correspond to the region in red box 2 in Figure 7a–c. In the SAR image in Figure 7i, most of the craters can be detected by YOLOv7. MRF can detect rocky areas and pixel-sized craters. But MRF cannot detect the crater walls that are facing away from the radar and exhibit low backscattering. Therefore, the slope angle map in Figure 7h can complement the detection results of MRF and YOLOv7. Most of the craters, central peaks, and rocky areas can be detected in Figure 7i. The rough areas are masked by red.

In box 1 of Figure 7g, there is no strong backscattering observed in the SAR image. But there are steep slopes in the slope angle map in Figure 7h. Slopes with low backscattering may face away from the radar. So, it can be detected from the slope angle map rather than the MRF in Figure 7i.

The deviation of the position of the same crater in box 2 in the SAR image and DEM data in Figure 7g–i is caused by the offset of the crater's position in SAR imaging. The fresh crater in box 3 can be detected from both the slope angle map and the SAR image. In addition, the SAR image can additionally detect the rocky ejecta blanket.

Furthermore, the detections of craters and rocky regions in the PSRs of craters Shackleton, Shoemaker, and Slater are presented as well.

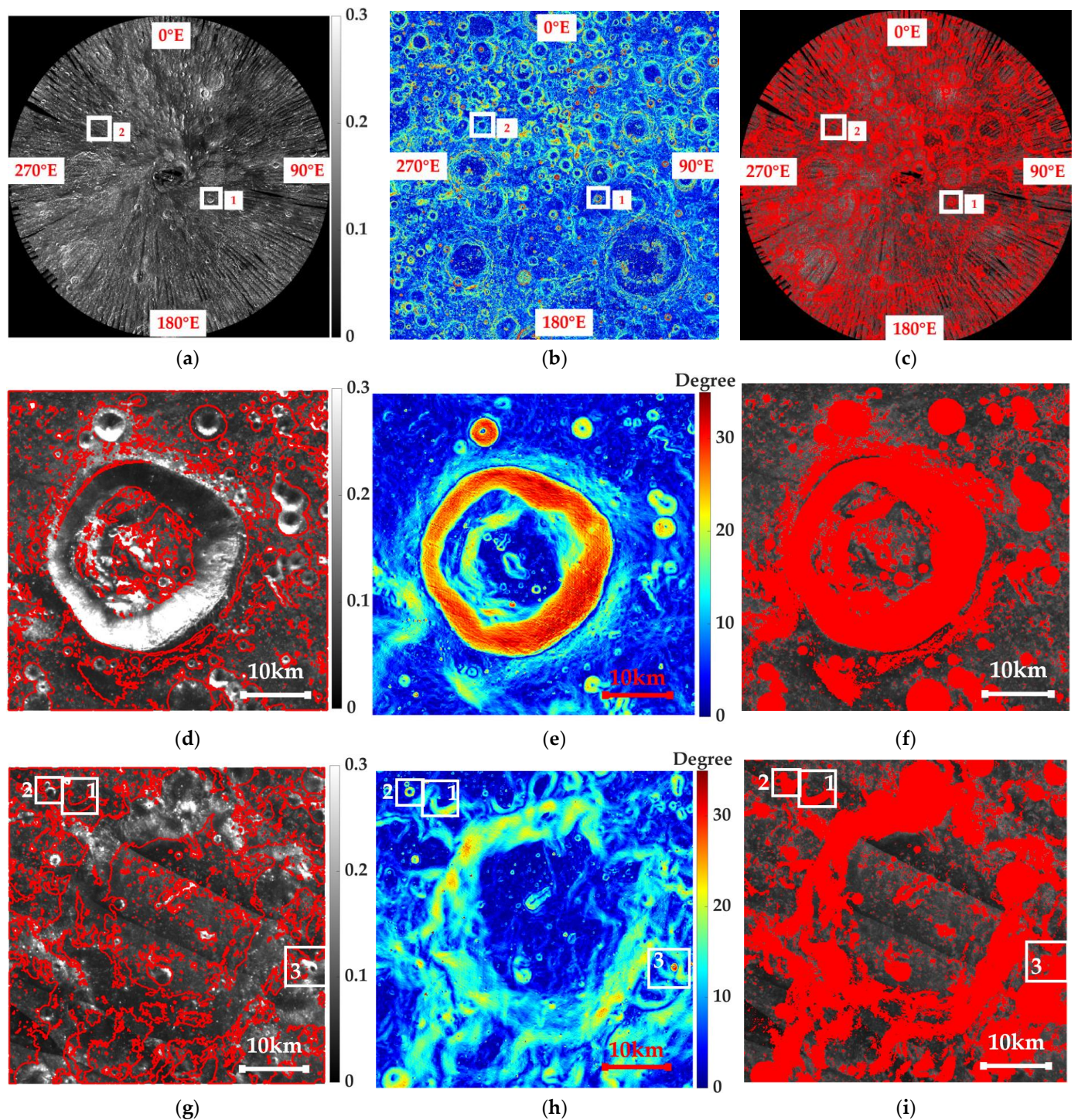


Figure 7. Detection results for the lunar south pole and selected regions: (a) the SAR image of the lunar south pole with a resolution of 118.45 m/pixel. (b) aligned DEM data with a resolution of 118.45 m/pixel. (c) the detection results of the lunar south pole in SAR images. In the image, red masks are the rough areas. (d) a zoomed-in image of box 1 of (a), which is crater Idel'son located at 84.02°S , 118.74°E , with a size of 400×400 pixels. (g) the enlarged image of box 2 of (a), which is located at 79.24°S , 304.31°E , with a size of 450×450 pixels. (e,h) the aligned DEM data in (d,g). (f,i) The red masks are the rough areas.

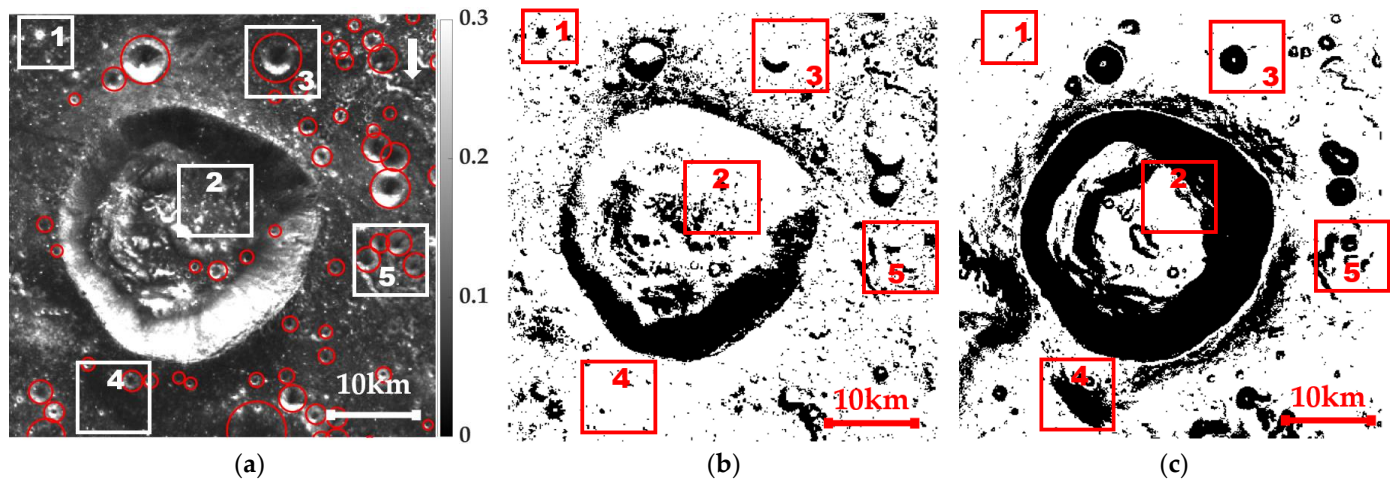


Figure 8. Magnified regions within box 1 in Figure 7a–c show the detection results of different methods: (a) Impact craters extracted by YOLOv7. The direction of the arrow in the top-right corner indicates the radar illumination direction. (b) Rough rock areas and pixel-sized impact craters detected by MRF. The black regions are rocky or steep regions. (c) Steep regions and the crater walls of large impact craters with slope angles greater than 10° extracted from the filtered DEM. The black regions are steep, and the white regions are flat.

3.1. Shackleton Crater

Crater Shackleton (89.50°S , 0.00°E) in Figure 1 is located at the lunar south pole, whose diameter is approximately 20 km [32]. The mini-fly in the Chang’e 7 mission will land in the PSR of the crater Shackleton [6].

Figure 9a is the SAR image of the crater Shackleton. The incidence angle of the radar is 32.4° . The slope angles of the crater walls range from 30° to 35° . In this region, there is a geometric distortion in the SAR image caused by changes in altitudes. In this case, a geometric correction with DEM data is necessary. The SAR image of crater Shackleton is geographically corrected based on DEM data [33]. The USGS-ISIS3 is utilized to register the DEM and SAR data [34]. ArcGIS Pro 3.0.0 software is used for the geometric correction of SAR images with transformation tools. Fifteen pairs of alignment points are manually selected and evenly distributed inside and outside the craters. The SAR image is registered to the DEM image by a spline function for accurate alignment. Figure 9b–d are the magnified images of the red box in Figure 9a. Large craters, pixel-sized craters, rocky areas, and radar-oriented slopes are detected with the YOLOv7 and MRF. Four craters were detected in the SAR image in Figure 9b by YOLOv7, and the diameters of the detected craters range from 0.22 to 0.35 km. The red lines in Figure 9b are the boundaries between rough and flat areas. The DEM data in Figure 9c are used to exclude steep crater walls with slope angles larger than 10° . Combining the detection results from the SAR image and slope angle map, rough regions are indicated with red masks in Figure 9d.

It can be observed that the regions in boxes 1, 2, 3, 4, and 5 are flat in the slope angle maps in Figure 9c. Backscattering from the flat regions in boxes 1, 3, 4, and 5 is low, indicating flat areas. However, it can be seen that the backscattering is strong at many discrete small regions in box 2 in Figure 9b, indicating these regions in box 2 are undulating. Both SAR images and DEM data play a unique role in the detection of flat regions in the PSRs. These selected flat regions in Figure 9d can provide references for the selection of landing sites for the Chang’e 7 mission.

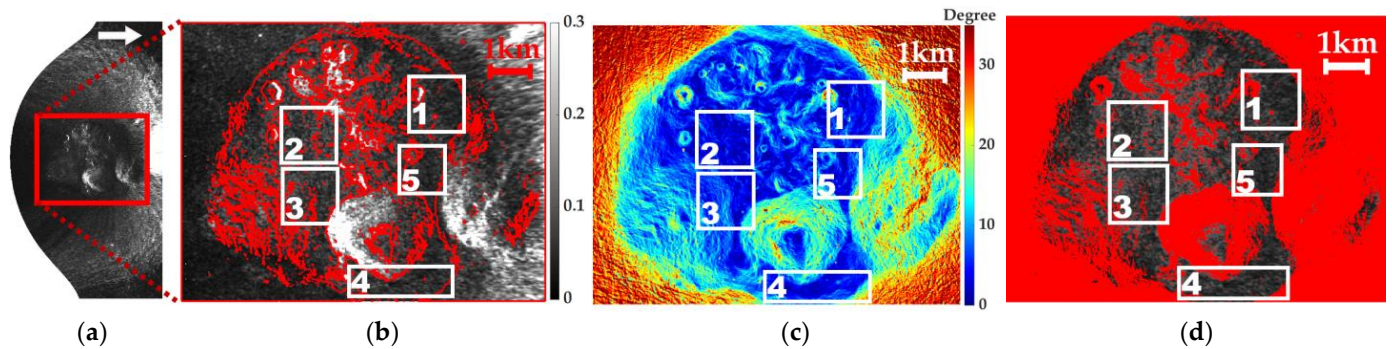


Figure 9. The detection result of the Shackleton crater floor: (a) the registered SAR image of the Shackleton crater floor with a resolution of 10 m/pixel. The white arrow indicates the direction of incidence. (b) a magnified portion within the red box on the crater floor in (a). The red lines are the boundaries between rough and flat areas. (c) the aligned slope angle map from DEM data. (d) the detection results. Red masks are the rough areas. The regions without masks are the flat areas.

3.2. Shoemaker Crater

Crater Shoemaker (88.14°S , 45.91°E) has a diameter of 52 km [32]. Figure 10a is the SAR image of the crater Shoemaker with an incidence angle of 51.4° . This image includes part of the crater wall and a flat crater floor. The spatial resolution of the SAR image is 14.8 m/pixel. The enlarged SAR image of the red box in Figure 10a is presented in Figure 10b to indicate the detailed topography. With YOLOv7, 27 craters are detected in the SAR image. The diameter of the craters ranges from 0.15 to 2.86 km. The aligned slope angle map from LOLA DEM data of 10 m/pixel is shown in Figure 10c. The rocky regions and craters are masked by red masks in Figure 10d.

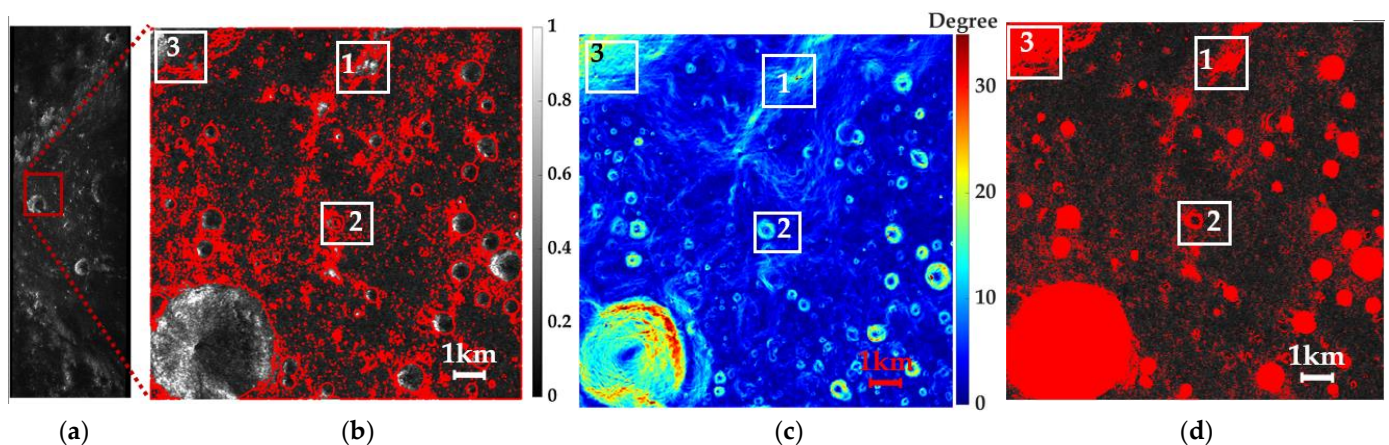


Figure 10. The detection result for a portion of the crater Shoemaker: (a) a SAR image of a partial crater Shoemaker (88.14°S , 45.91°E) with a resolution of 14.8 m/pixel. (b) the enlarged region of the red box. (c) the slope angle map from DEM data. (d) the detection results. Red masks represent the rocky areas.

In the SAR image of Figure 10b, large craters, pixel-sized craters, rocky regions, and other undulations can be detected by the YOLOv7 and MRF algorithms. In box 1 of Figure 10c, there is a strip-shaped undulation region with a slope angle smaller than 10° in the slope angle map, making it difficult to detect in DEM data. However, from the SAR image, this area has strong backscattering, which can be detected with MRF. The small crater in box 2 is not detected by YOLOv7. The MRF algorithm and the slope angle map can only detect the crater walls. So, the crater floor of the small crater in box 2 is not indicated by red in Figure 10d. The backscattering is weak at box 3 in Figure 10b. But the slope angle in this region is greater than 10° on the slope angle map. It can be found that this

region faces away from radar. Therefore, this region is not detectable in SAR images. The slope angle map is helpful in detecting these regions. The regions without a red mask in Figure 10d are relatively flat regions suitable for landing.

3.3. Slater Crater

Crater Slater is located at 88.08°S , 111.29°E . The SAR image of the crater floor with an incidence angle of 30.8° is shown in Figure 11a. The resolution of the SAR image and the slope angle map is 14.8 m/pixel. Figure 11b presents the zoomed-in data of the red box in Figure 11a. A total of 44 craters are detected by YOLOv7, with diameters ranging from 0.21 to 1.39 km. The red lines in Figure 10b are the boundaries of the flat and rough regions. The aligned slope angle map in Figure 11c is derived from LOLA DEM data at 10 m/pixel. Large craters, pixel-sized craters, rocky areas, and other steep slopes can be detected in Figure 11d and are indicated in red.

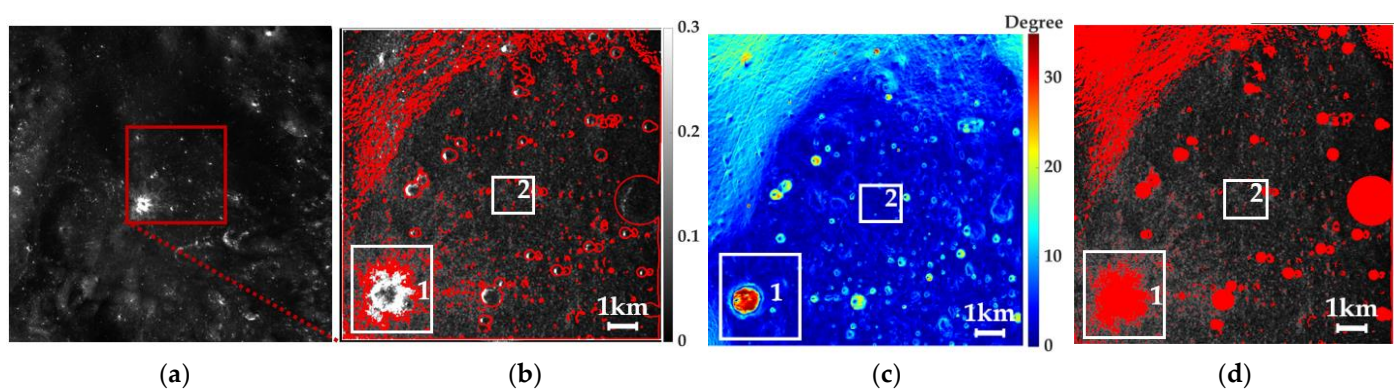


Figure 11. The detection result for a part of the crater Slater: (a) SAR image of crater Slater (88.08°S , 111.29°E) with a resolution of 14.8 m/pixel. (b) the region within the red box in (a). The red lines are the boundaries of the flat and rough regions. (c) the slope angle map with a resolution of 14.8 m/pixel. (d) the detection results. Red masks represent the relative rocky areas.

In box 1 in Figure 11c, a small crater can be detected. However, it can be seen that there are rocky ejecta blankets around this crater in Figure 11b, which cannot be detected from Figure 11c. The rocky ejecta blankets can be detected in SAR image in Figure 11b. In box 2 in Figure 11c, the slope angles of this region are approximately 0° . But there are some pixel-sized craters that can be detected in an SAR image with MRF. The relatively flat regions suitable for landing are indicated in red in Figure 11d.

4. Conclusions

In this paper, the YOLOv7 and MRF algorithms are applied to identifying large and small craters, surface rocks, and other undulating terrain surfaces in SAR images. These identifications of the lunar morphology are validated in comparison with the optical images. Based on the SAR image and DEM data as available, YOLOv7 and MRF can classify the distributions of surface rocks and large and small crater regions in the PSRs and exclude regions with a slope angle larger than 10° . The smooth regions suitable for landing missions can then be established. This detection is applied to the craters Shackleton, Shoemaker, and Slater as a reference and landing guidance for future landing missions.

Author Contributions: Conceptualization, N.L., F.X. and Y.-Q.J.; methodology, N.L. and T.X.; validation, T.X. and X.R.; formal analysis, T.X.; investigation, T.X.; data curation, T.X., X.R. and Y.L.; writing—original draft preparation, T.X. and X.R.; writing—review and editing, N.L., T.X., X.R. and Y.-Q.J.; visualization, T.X.; supervision, N.L. and Y.-Q.J.; funding acquisition, N.L. All authors have read and agreed to the published version of the manuscript.

Funding: This research is funded by the National Natural Science Foundation of China under Grant 62201154 and FDUROP (Fudan Undergraduate Research Opportunities Program) (23202).

Data Availability Statement: The Mini-RF, lunar orbiter laser altimeter (LOLA), and lunar reconnaissance orbiter camera (LROC) data used in this study are publicly available on <http://pds-geosciences.wustl.edu> and <https://quickmap.lroc.asu.edu/>.

Acknowledgments: The Mini-RF, lunar orbiter laser altimeter (LOLA), and lunar reconnaissance orbiter camera (LROC) data used in this study are publicly available from <http://pds-geosciences.wustl.edu> accessed on 10 September 2023 and <https://quickmap.lroc.asu.edu/> accessed on 10 September 2023. The MMDetection platform is available online at <https://github.com/open-mmlab/mmdetection> accessed on 10 April 2024. We thank Hecheng Jia, Zhenwei Xin, and Zhengling Yin for their sincere advice on this paper.

Conflicts of Interest: The authors declare no conflicts of interest.

References

1. Watson-Morgan, L.; Chavers, G.; Connolly, J.; Crowe, K.; Krupp, D.; Means, L.; Percy, T.; Polsgrove, T.; Turpin, J. NASA's Initial and Sustained Artemis Human Landing Systems. In Proceedings of the 2021 IEEE Aerospace Conference (50100), Big Sky, MT, USA, 6–13 March 2021; pp. 1–11.
2. Creech, S.; Guidi, J.; Elburn, D. Artemis: An Overview of NASA's Activities to Return Humans to the Moon. In Proceedings of the 2022 IEEE Aerospace Conference (AERO), Big Sky, MT, USA, 5–12 March 2022; pp. 1–7.
3. Liu, J.; Zeng, X.; Li, C.; Ren, X.; Yan, W.; Tan, X.; Zhang, X.; Chen, W.; Zuo, W.; Liu, Y.; et al. Landing Site Selection and Overview of China's Lunar Landing Missions. *Space Sci. Rev.* **2020**, *217*, 6. [[CrossRef](#)]
4. Zheng, Y.; Ouyang, Z.; Li, C.; Liu, J.; Zou, Y. China's Lunar Exploration Program: Present and future. *Planet. Space Sci.* **2008**, *56*, 881–886. [[CrossRef](#)]
5. Yin, Z.; Liu, N.; Jin, Y. Simulation of the temperatures in the permanently shadowed region of the Moon's south pole and data validation. *Icarus* **2023**, *411*, 115917. [[CrossRef](#)]
6. Chi, W.; Yingzhuo, J.; Changbin, X.; Yangting, L.; Jianzhong, L.; Xiaohui, F.; Lin, X.; Yun, H.; Yufen, Z.; Yigang, X.; et al. Scientific objectives and payload configuration of the Chang'E-7 mission. *Natl. Sci. Rev.* **2023**, *11*, nwad329. [[CrossRef](#)] [[PubMed](#)]
7. Smith, D.E.; Zuber, M.T.; Neumann, G.A.; Mazarico, E.; Lemoine, F.G.; Head Iii, J.W.; Lucey, P.G.; Aharonson, O.; Robinson, M.S.; Sun, X.; et al. Summary of the results from the lunar orbiter laser altimeter after seven years in lunar orbit. *Icarus* **2017**, *283*, 70–91. [[CrossRef](#)]
8. Liu, N.; Jin, Y.-Q. Selection of a Landing Site in the Permanently Shadowed Portion of Lunar Polar Regions Using DEM and Mini-RF Data. *IEEE Geosci. Remote Sens. Lett.* **2022**, *19*, 4503305. [[CrossRef](#)]
9. Liu, N.; Jin, Y.-Q. Pol-SAR Image Simulation of the Lunar Surface with Data Analysis of Chandrayaan-2 and Mini-RF. *IEEE J. Sel. Top. Appl. Earth Obs. Remote Sens.* **2023**, *16*, 10301–10310. [[CrossRef](#)]
10. Liu, N.; Jin, Y.-Q. Simulation of Pol-SAR Imaging and Data Analysis of Mini-RF Observation From the Lunar Surface. *IEEE Trans. Geosci. Remote Sens.* **2022**, *60*, 2000411. [[CrossRef](#)]
11. Liu, N.; Xu, F.; Jin, Y.-Q. A Numerical Model of CPR of Rough Surface With Discrete Scatterers for Analysis of Mini-RF Data. *Radio Sci.* **2020**, *55*, e2018RS006776. [[CrossRef](#)]
12. Chang, S.; Deng, Y.; Zhang, Y.; Zhao, Q.; Wang, R.; Zhang, K. An Advanced Scheme for Range Ambiguity Suppression of Spaceborne SAR Based on Blind Source Separation. *IEEE Trans. Geosci. Remote Sens.* **2022**, *60*, 5230112. [[CrossRef](#)]
13. Gao, Y.; Zhao, F.; Hou, W.; Han, Y.; Liu, M.; Dang, Y.; Lu, P.; Wang, R. Analysis of Rock Abundance on Lunar Surface and Near-Surface Using Mini-RF SAR Data. *IEEE J. Sel. Top. Appl. Earth Obs. Remote Sens.* **2023**, *16*, 9590–9605. [[CrossRef](#)]
14. Raney, R.K.; Spudis, P.D.; Bussey, B.; Crusan, J.; Jensen, J.R.; Marinelli, W.; McKerracher, P.; Neish, C.; Palsetia, M.; Schulze, R.; et al. The Lunar Mini-RF Radars: Hybrid Polarimetric Architecture and Initial Results. *Proc. IEEE* **2011**, *99*, 808–823. [[CrossRef](#)]
15. Kereszturi, A.; Tomka, R.; Steinmann, V. Testing statistical impact crater analysis in permanently shadowed lunar polar regions. *Icarus* **2022**, *376*, 114879. [[CrossRef](#)]
16. Duda, R.O.; Hart, P.E. Use of the Hough transformation to detect lines and curves in pictures. *Commun. ACM* **1972**, *15*, 11–15. [[CrossRef](#)]
17. Chen, S.; Wang, H.; Xu, F.; Jin, Y.-Q. Target Classification Using the Deep Convolutional Networks for SAR Images. *IEEE Trans. Geosci. Remote Sens.* **2016**, *54*, 4806–4817. [[CrossRef](#)]
18. Wang, C.Y.; Bochkovskiy, A.; Liao, H.Y.M. YOLOv7: Trainable Bag-of-Freebies Sets New State-of-the-Art for Real-Time Object Detectors. In Proceedings of the 2023 IEEE/CVF Conference on Computer Vision and Pattern Recognition (CVPR), Vancouver, BC, Canada, 17–24 June 2023; pp. 7464–7475.
19. Jin, Y.-Q. Change Detection from Multi-Temporal SAR Images. In *Polarimetric Scattering and SAR Information Retrieval*; Wiley-IEEE Press: Hoboken, NJ, USA, 2013; pp. 291–309. [[CrossRef](#)]
20. Geman, S.; Geman, D. Stochastic Relaxation, Gibbs Distributions, and the Bayesian Restoration of Images. *IEEE Trans. Pattern Anal. Mach. Intell.* **1984**, *PAMI-6*, 721–741. [[CrossRef](#)]
21. Xi, L.H.; Hou, J.W.; Ma, G.L.; Hei, Y.Q.; Li, W.T. A Multiscale Information Fusion Network Based on PixelShuffle Integrated With YOLO for Aerial Remote Sensing Object Detection. *IEEE Geosci. Remote Sens. Lett.* **2024**, *21*, 7501505. [[CrossRef](#)]

22. Robinson, M.S.; Brylow, S.M.; Tschimmel, M.; Humm, D.; Lawrence, S.J.; Thomas, P.C.; Denevi, B.W.; Bowman-Cisneros, E.; Zerr, J.; Ravine, M.A.; et al. Lunar Reconnaissance Orbiter Camera (LROC) Instrument Overview. *Space Sci. Rev.* **2010**, *150*, 81–124. [[CrossRef](#)]
23. Zhou, Z.-H. *Machine Learning*; Springer: Singapore, 2021; p. XIII, 459. [[CrossRef](#)]
24. Xia, G.-S.; He, C.; Sun, H. A Rapid and Automatic MRF-Based Clustering Method for SAR Images. *IEEE Geosci. Remote Sens. Lett.* **2007**, *4*, 596–600. [[CrossRef](#)]
25. Bruzzone, L.; Prieto, D.F. Automatic analysis of the difference image for unsupervised change detection. *IEEE Trans. Geosci. Remote Sens.* **2000**, *38*, 1171–1182. [[CrossRef](#)]
26. Ren, S.; He, K.; Girshick, R.; Sun, J. Faster R-CNN: Towards Real-Time Object Detection with Region Proposal Networks. *IEEE Trans. Pattern Anal. Mach. Intell.* **2017**, *39*, 1137–1149. [[CrossRef](#)] [[PubMed](#)]
27. Cai, Z.; Vasconcelos, N. Cascade R-CNN: Delving Into High Quality Object Detection. In Proceedings of the 2018 IEEE/CVF Conference on Computer Vision and Pattern Recognition, Salt Lake City, UT, USA, 18–23 June 2018; pp. 6154–6162.
28. Ge, Z.; Liu, S.; Wang, F.; Li, Z.; Sun, J. YOLOX: Exceeding YOLO Series in 2021. *arXiv* **2021**, arXiv:2107.08430.
29. Chen, K.; Wang, J.; Pang, J.; Cao, Y.; Xiong, Y.; Li, X.; Sun, S.; Feng, W.; Liu, Z.; Xu, J.; et al. MMDetection: Open MMLab Detection Toolbox and Benchmark. *arXiv* **2019**, arXiv:1906.07155.
30. Wei, G.; Li, X.; Zhang, W.; Tian, Y.; Jiang, S.; Wang, C.; Ma, J. Illumination conditions near the Moon’s south pole: Implication for a concept design of China’s Chang’E–7 lunar polar exploration. *Acta Astronaut.* **2023**, *208*, 74–81. [[CrossRef](#)]
31. Li, S.; Jiang, X.; Tao, T. Guidance Summary and Assessment of the Chang’e-3 Powered Descent and Landing. *J. Spacecr. Rocket.* **2016**, *53*, 258–277. [[CrossRef](#)]
32. Tye, A.R.; Fassett, C.I.; Head, J.W.; Mazarico, E.; Basilevsky, A.T.; Neumann, G.A.; Smith, D.E.; Zuber, M.T. The age of lunar south circumpolar craters Haworth, Shoemaker, Faustini, and Shackleton: Implications for regional geology, surface processes, and volatile sequestration. *Icarus* **2015**, *255*, 70–77. [[CrossRef](#)]
33. Kirk, R.L. Radargrammetry with Chandrayaan-1 and LRO Mini-RF images of the Moon: Controlled mosaics and DTMs. *Eur. Planet. Sci. Congr. 2010* **2010**, *5*, 703.
34. Fassett, C.I.; Bramson, A.M.; Cahill, J.T.S.; Harris, C.P.; Morgan, G.A.; Neish, C.D.; Nypaver, C.A.; Patterson, G.W.; Rivera-Valentin, E.G.; Taylor, P.A.; et al. Improved Orthorectification and Empirical Reduction of Topographic Effects in Monostatic Mini-RF S-band Observations of the Moon. *Planet. Sci. J.* **2024**, *5*, 4. [[CrossRef](#)]

Disclaimer/Publisher’s Note: The statements, opinions and data contained in all publications are solely those of the individual author(s) and contributor(s) and not of MDPI and/or the editor(s). MDPI and/or the editor(s) disclaim responsibility for any injury to people or property resulting from any ideas, methods, instructions or products referred to in the content.